Hindawi
Journal of Advanced Transportation
Volume 2022, Article ID 8653547, 18 pages
https://doi.org/10.1155/2022/8653547

Research Article

Active Equalization Strategy for Lithium-Ion Battery Packs Based on Multilayer Dual Interleaved Inductor Circuits in Electric Vehicles

Xu Lei, Jianping He, Linqian Fan, and Guiping Wang

School of Electronics and Control Engineering, Chang'an University, Xi'an 710064, China

Correspondence should be addressed to Xu Lei; xulei@chd.edu.cn

Received 21 October 2021; Revised 14 February 2022; Accepted 3 March 2022; Published 20 March 2022

Academic Editor: Luca D'Acierno

Lithium-ion batteries (LIBs) are widely used in electric vehicles (EVs) due to their superior power performance over other batteries. However, when connected in series, overcharged cells of LIBs face the risk of explosion, and undercharged cells decrease the life cycle of the battery. Eventually, the inconsistency phenomenon between cells resulting from manufacturing tolerance and usage process reduces the overall charging capacity of the battery and increases the risk of explosion after long-time use. Research has focused on synthesizing active material to achieve higher energy density and extended life cycle for LIBs while neglecting a comparative analysis of equalization technology on the performance of battery packs. In this paper, a nondissipative equalization structure is proposed to reconcile the inconsistency of series-connected LIB cells. In this structure, a circuit uses high-level equalization units to enable direct energy transfer between any two individual cells, and dual interleaved inductors in each equalization unit increase the equalization speed of a single cell in one equalization cycle by a factor of two. The circuit is compared with the classical inductor equalization circuit (CIEC), dual interleaved equalization circuit (DIEC), and parallel architecture equalization circuit (PAEC) in the states of standing, charging, and discharging, respectively, to validate the advantages of the proposed scheme. Considering the diversity of imbalance states, the state of charge (SOC) and terminal voltage are both chosen as the equalization criterion. The second-order RC model of the LIB and the adaptive unscented Kalman filter (AUKF) algorithm are employed for SOC estimation. For effective equalization, the adaptive fuzzy neural network (AFNN) is utilized to further reduce energy consumption and equalization time. The experiment results show that the AFNN algorithm reduces the total equalization time by approximately 37.4% and improves equalization efficiency by about 4.89% in contrast with the conventional mean-difference algorithm. Particularly, the experiment results of the equalization circuit verification certify that the proposed equalization structure can greatly accelerate the equalization progress and reduce the equalization loss compared to the other three equalization circuits.

1. Introduction

EVs have attracted increasing attention in recent years due to their efficient energy utilization, zero emissions, and contributions to carbon neutral and green global environment. EVs commonly use LIBs characterized by superior power performance, long life, high-energy density, and no memory effect [1, 2]. However, the electrical capacity, voltage, and instantaneous discharge power of individual LIB cell are far below electricity demand in real-world applications. Thus, LIB cells are often connected in series to boost the voltage and in parallel to increase the capacity [3].

Different from cells connected in parallel that are able to self-balance the charge, cells connected in series are faced with the problem of cell charge imbalance that worsen over time [3–5]. In Figure 1, multiple cells are connected in series to form a string with a high voltage level. The charge of cells differs owing to the capacity, self-discharge rate, internal impedance, and temperature mismatch. Manufacturing differences and discrepancies in the usage environment reduce the overall battery performance, which accelerates battery aging and causes safety hazards (e.g., a fire or, in the worst case, an explosion) [6–8]. These issues are worsened by the fact that LIBs are very sensitive to deep discharge and

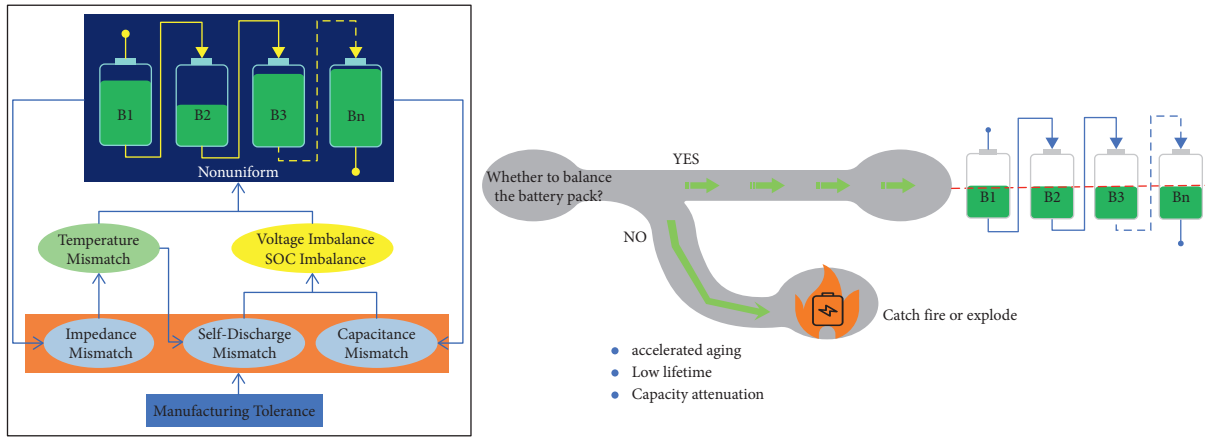

Figure 1: Sources of nonuniform, performance, and an equalization system design. B_i denotes the (i)-th battery cell.

overcharge [9]. Numerous studies have been conducted to improve the capacity and life cycle of LIBs, and the safety issues have not been well addressed [10]. Manufacturing differences are inevitable, and thus a proper equalization technology is needed to make each cell operate safely and reliably.

The essence of equalization technology is to lower as much as possible the charge variance by equalization circuits and equalization control algorithms. The equalization technology is classified into passive and active according to the energy consumption and energy transfer [11]. The passive equalization technology dissipates the excess power of a higher SOC cell by power resistors, and yet it has two distinct drawbacks: energy waste and thermal imbalance. The delayed thermal consumption results in high local temperature of the battery pack, which may be a safety hazard [12]. The active equalization technology solves these two drawbacks by moving the excess power from higher SOC cells to lower ones via capacitors, inductors, or transformers [12]. The charge imbalance is resolved by energy deallocation. Particularly, the inductor-based active equalization circuit has wide acceptance because of good controllability and reliability [13]. In this paper, based on the CIEC, an inductor-based multilayer dual interleaved equalization circuit (MLDIEC) is proposed. The MLDIEC avoids inefficient transmission of energy when two battery cells are far apart with the aid of a high-level equalization unit. Incorporating dual interleaved inductors into the circuit enhances the equalization efficiency. Meanwhile, theoretical calculations are carried out to explore the relationship among different equalization parameters.

An equalization control strategy complementary to the equalization circuit is presented to illustrate the equalization processes. Generally, equalization control strategies can be based on the terminal voltage, SOC, or capacity, depending on the battery characteristics. Note that these variables can also be used as criteria to determine whether the battery pack is balanced. The terminal voltage of the battery is measurable in real time with a simple monitoring system, but it cannot describe the charge in the SOC-open-circuit voltage (OCV) plateau accurately [14]. The SOC takes into account many factors (e.g., the voltage, current, and internal resistance environmental temperature), yet it cannot be measured directly. Instead, the SOC needs to be calculated with various methods, e.g., the electrochemical model, the equivalent circuit method, and neural networks. The complexity of these methods limits their applicability of the SOC-based strategy [13]. The capacity-based strategy considers the aging rate besides SOC. Yet, the battery capacity is only available offline, and thus this method is not suitable for real-time applications [11]. In practice, the terminal voltage and SOC are adopted in different regions of the SOC-OCV characteristic curve of LIBs [15]. In the low and high voltage regions of the curve, the terminal voltage-based strategy is adopted to prevent overcharging or discharging [16]. In the plateau region, the SOC-based strategy is preferred since it describes the battery charge accurately. To achieve high accuracy in real-time applications, the SOC value can be estimated by the Kalman filter algorithm based on an equivalent circuit model. The improved unscented Kalman filter (UKF) proposed by J. C Lv estimates SOC with the error of just 0.63% [17, 18]. Thus, the AUKF is employed for SOC estimation.

The equalization control strategy incorporates an equalization algorithm [19, 20]. The mean-difference algorithm is widely applied to the inductor-based equalization circuit due to its simplicity. However, the mean-difference algorithm is inefficient since it cannot maximize the overall performance of the equalization circuit [21]. Therefore, we employ the AFNN to develop the equalization algorithm. This algorithm is suitable for real-time operations, is very adaptive, and realizes nonlinear mapping with arbitrary accuracy. Thus, the AFNN is suitable for complex controlled objects that are challenging to be described by a mathematical model of the battery pack [22].

Figure 2 shows the overall structure of the proposed MLDIEC and its control strategy. The SOCs and terminal voltages of cells marked in the diagram are chosen to judge the equalization status of the battery pack. The AUKF is used for SOC estimation. The AFNN is adopted to improve the equalization efficiency. The rest of this paper is organized as follows. Section 2 introduces the structure and operating

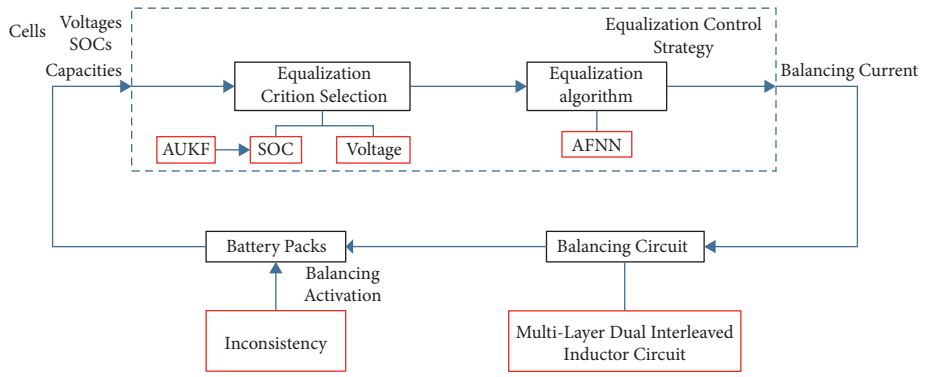

Figure 2: Overall structure of the proposed MLDIEC and its control strategy.

principle of the MLDIEC. Section 3 describes the AUKF to estimate the SOC. Section 4 presents the equalization control algorithm in detail. Section 5 presents the experiment results. Section 6 concludes the paper.

2. The MLDIEC

[23] proposes a CIEC, where an inductor is put between two adjacent cells to transfer energy from a high SOC cell to a low SOC cell, as illustrated in Figure 3. However, the energy transfer is limited to adjacent cells. Bo Dong et al. [4] proposed a multilayer inductor equalization circuit (MLIEC). With this circuit, energy is exchanged directly between two cells far apart, avoiding intermediate inductors and reducing energy loss during equalization [24, 25]. Inductors in the CIEC and MLIEC are operated with asynchronous current to prevent inductor saturation but make inductor inefficient during equalization [26]. To overcome this drawback, we propose a multilayer dual interleaved equalization circuit (MLDIEC) based on the MLIEC, as shown in Figure 4(a).

Figure 4(b) shows an equalization unit $EU1$-1 in greater detail, including two inductors ($L1$ and $L2$) and four MOSFETs ($S1$, $S2$, $S3$, and $S4$). High-layer units are utilized to transfer energy between any two cells, which speeds up the equalization, increases the battery energy usage, and reduces energy loss. The dual inductors replace the conventional single inductor and increase the cell operating time during an equalization cycle. This way, the circuit avoids keeping the battery idle for a long time and increases the equalization speed. The layer number and unit number per layer are determined by equations (1) and (2), respectively:

$$m = [\log_2 n] + 1,$$
$$a = \frac{[\log_2 n]}{i}, \quad (1)$$

where m is the number of equalization layers, n is the number of cells in the series-connected battery, $[-]$ represents the Gaussian rounding function, and a is the number of equalization units in layer i.

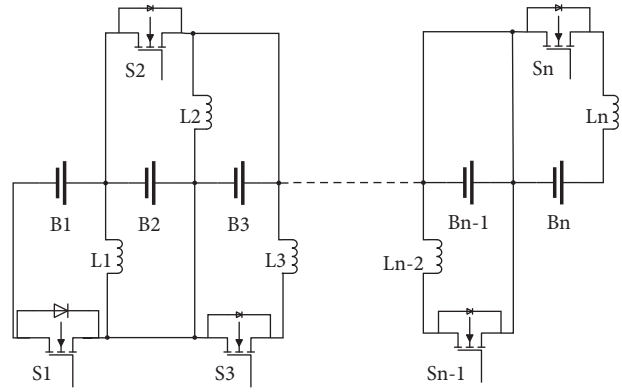

Figure 3: Classical inductor equalization circuit topology.

2.1. Working Principle. The equalization unit is a dual interleaved inductor unit that increases the cell operating time in an equalization cycle. Yet, a battery cell cannot be charged and discharged to two inductors simultaneously, which reduces the energy transfer efficiency. To address this issue, the phase difference between the pulse width modulation (PWM) signals of the two inductors can be set to 180°, so that the two inductors can compensate each other, and the battery operates safely. Take the $EU1$-1 in Figure 4(b) as an example. The two inductors work in Discontinuous Conduction Mode (DCM), and their operations are the same [27]. Assume that the SOC of $B1$ is higher than that of $B2$ to analyze the operating state of inductor $L1$. The equalization control switch $S1$ is controlled to achieve battery equalization at first. The equalization process within an equalization cycle T is divided into three stages based on the direction of energy transfer. The signal waveform of the three stages is shown in Figure 5, and the D is the duty cycle.

Stage 1: (0-$t_1(DT)$).

When the control signal from the equalization control system is set, switch $S1$ is turned on. Battery $B1$, inductor $L1$, and switch $S1$ make up a closed loop. The electric energy is converted into magnetic energy and stored in $L1$. According to the Kirchhoff laws (KCLs), the voltage relationship of the loop is obtained by

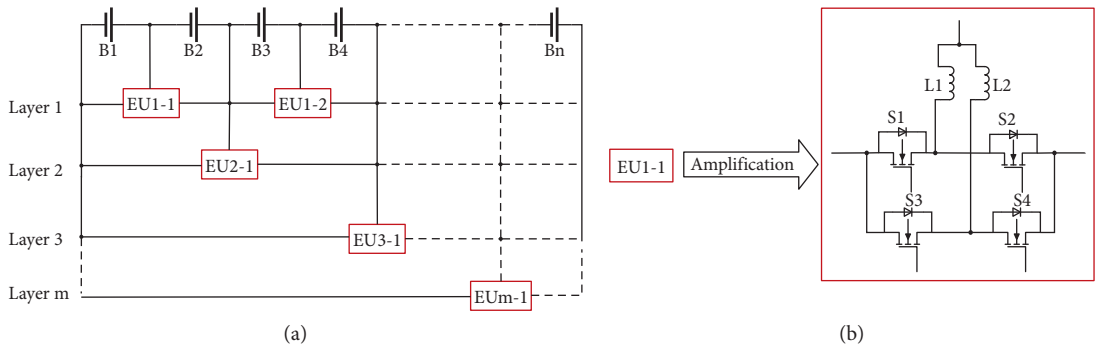

Figure 4: (a) The equalization circuit topology; (b) the enlargement of the proposed equalization unit *EU*1-1.

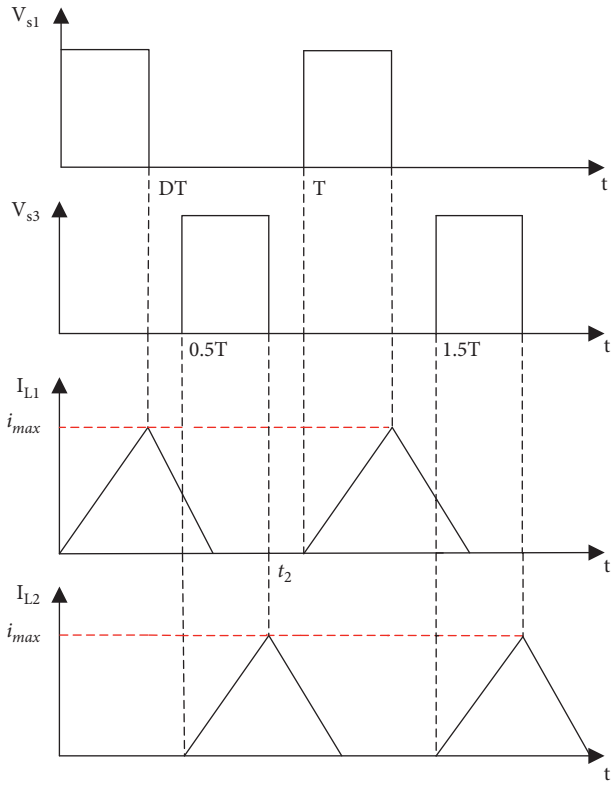

Figure 5: Signal waveform of inductors (L)1 and (L)2.

$$R_{T-on}i(t) + L_1\frac{di(t)}{dt} = V_{B1}. \tag{2}$$

The current of $L1$ is as follows:

$$i(t) = \frac{V_{B1}}{R_{T-on}}\left(1 - e^{-R_{T-on}/L_1 t}\right), \tag{3}$$

where $R_{T\text{-}on}$ is the total equivalent resistance of $L1$, $S1$, and $B1$ and the wire when $S1$ is turned on, L_1 is the inductance of $L1$, and V_{B1} is the battery voltage, which can be regarded as constant because the voltage does not vary much during a single period. When t reaches t_1, $B1$ finishes discharging. The current of $L1$ reaches the maximum value in this equalization cycle.

Stage 2: (t_1-t_2).

When switch $S1$ is turned off, a loop consists of $B2$, $L1$, and $S2$ is formed. At this stage, the magnetic energy stored in $L1$ is released. Similarly, the voltage of the loop is given by

$$R_{T-off}i(t) + V_{B2} = L_1\frac{di(t)}{dt} + V_D. \tag{4}$$

The current of $L1$ is found to be

$$i(t) = e^{-R_{T-on}/L_1\left(t-t_1\right)}i_{\max} + \frac{V_{B2} - V_D}{R_T}\left(e^{-R_{T-on}/L_1\left(t-t_1\right)} - t\right), \tag{5}$$

where $R_{T\text{-}off}$ is the equivalent internal resistance sum of $L1$, $B2$ and the wire when $S1$ is turned off, which can be approximately as $R_{T\text{-}off} = R_{T\text{-}on} = R_T$, V_{B2} is the voltage value of $B2$ but is a constant, and V_D is the on-state voltage drop of the parasitic diode of MOSFET $S2$ [28].

At time 0.5 T, switch $S3$ is turned on. Another loop is made up of $B1$, $L2$, $S3$. The electric energy of $B1$ is converted into magnetic energy, and stored in $L2$.

Stage 3: (t_2-T).

At the end of stage 2, all the energy of inductor $L1$ transfers to $B2$. Stage 3 aims to prevent stage 1 of the next cycle from overlapping with stage 2 of the current period, which avoids energy accumulation in inductors.

2.2. Equalization Circuit Parameters

2.2.1. PWM Duty Cycle. To ensure that the inductor equalization unit operates in DCM, the PWM duty cycle of the MOSFET needs to avoid energy accumulation. Equations (3) and (5) describe the voltage relationship during the discharging and charging operations. Ignoring the equivalent resistance $R_{T\text{-}on}$ and the MOSFET on-state voltage drop

V_D in the two equations, the current of $L1$ is changed as follows:

$$\begin{cases} i(t) = \dfrac{V_{B1}}{L_1} t, & (0 < t < t_1), \\ i(t) = \dfrac{V_{B1}}{L_1} t_1 - \dfrac{V_{B2}}{L_1} (t - t_1), & (t_1 < t < t_2). \end{cases} \tag{6}$$

Assuming that t is equal to T, the duty cycle D and voltages should meet the following requirement:

$$\frac{V_{B1}}{L_1} DT - \frac{V_{B2}}{L_1} (1 - D)T \le 0. \tag{7}$$

A relationship between D and voltages is thus developed as

$$D \le \frac{V_{B2}}{V_{B1} + V_{B2}}. \tag{8}$$

To make the inductor in DCM, V_{B2} should equal V_{B1}. Therefore, the maximum theoretical value of duty cycle D is 0.5. Furthermore, based on the inductors operated in DCM and the current of $L1$ in one equalization cycle, the maximum energy transfer ratio of an individual inductor in the first-level equalization unit can be formulated as

$$Q_V = \frac{V_{B1} D^2 T}{2 L_1 f}, \tag{9}$$

where Q_v can also be interpreted as the average current value of the inductor, and f is the switching frequency.

2.2.2. Inductor and Square Wave Frequency. To avoid battery damage from excessive current during equalization, the maximum current supplied to the battery should be below the peak current. The equalization circuit is designed as a hierarchical structure by considering that the current of different layers may superimpose on the battery. The inductor peak current of the equalization unit per layer is the same as that of the first layer. Thus, we obtain

$$\frac{i_{B-\text{Define}}}{m} \ge \frac{V_{B-\text{MAX}} D}{Lf}, \tag{10}$$

where $V_{B\text{-}MAX}$ is the upper limit voltage, $i_{B\text{-}Define}$ is the maximum equalization current allowed, m is the number of equalization layers, and f is the square wave frequency reflecting the relationship between the switching frequency of the MOSFET and the losses during equalization.

2.2.3. Switching Voltage. The MOSFET employs switching frequency to control the current during equalization. The maximum withstanding voltage of the MOSFET must be greater than the voltage applied at both ends, preventing it from breaking down. As seen in Figure 5, the voltage across the MOSFET at the disconnection moment is the battery voltage. However, the MOSFET in each layer withstands the different voltage, increasing with the number of layers. The maximum withstand voltage of the MOSFET is

$$V_{\text{stress}} = V_{\max} 2^{m-1}, \tag{11}$$

where $V_{\max}$ is the maximum voltage of an individual cell, and m is the number of equalization layers.

3. SOC Estimation Based on AUKF

The SOC estimation accuracy is directly affected by the performance of the equalization control algorithm. To make an accurate estimation, this paper employs a second-order equivalent circuit model considering the battery hysteresis effect and uses AUKF to estimate the SOC. The Kalman filter algorithm combined with the second-order equivalent circuit model estimates the SOC accurately in real-time applications. Meanwhile, the extended Kalman filter (EKF) and cubature Kalman filter (CKF) are employed as benchmarks.

3.1. Second-Order Equivalent Circuit Model. Much effort has gone into building battery models, such as the equivalent circuit model, the neural network model, and the electrochemical model. The equivalent circuit model can better respond to the relationship between battery parameters, reflect the dynamic performance of the battery, and facilitate the battery characteristics analysis and parameter identification [26, 29]. Here, we propose a second-order RC equivalent circuit model with hysteresis effects. The two RC networks shown in Figure 6 describe the effects of differential polarization and electrochemical polarization, respectively.

Let $Uoc(t)$ be the battery OCV. $R0$ denotes the ohmic internal resistance of the battery [12]. There are four parameters in the two RC networks. Re and Ce denote the electrochemical polarization internal resistance and capacitance of the battery, respectively. Rd and Cd denote the concentration polarization resistance and capacitance, respectively. $I(t)$ is the dry circuit current, positive for discharging and negative for charging.

According to KCL and Kirchhoff's Voltage Law (KVL), the ohmic voltage $U_0(t)$, the electrochemical polarization voltage $U_e(t)$, and the concentration polarization voltage $U_d(t)$ can be calculated by

$$\begin{cases} U_0(t) = R_0 I(t), \\ U_e(t) = R_e \left(I(t) - C_e \dfrac{dU_e(t)}{dt} \right), \\ U_d(t) = R_d \left(I(t) - C_e \dfrac{dU_d(t)}{dt} \right). \end{cases} \tag{12}$$

respectively. And the battery terminal voltage $U(t)$ is

$$U(t) = U_{OC}(t) + U_O(t) + U_e(t) + U_d(t). \tag{13}$$

By the current integration method, we have

$$\text{SOC}(t) = \text{SOC}_0 - \frac{1}{Q_N} \int_0^t \eta I(t) \mathrm{d}t. \tag{14}$$

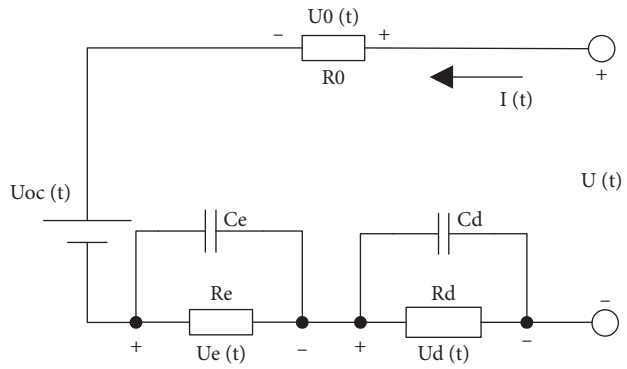

Figure 6: Second-order RC equivalent circuit model.

where SOC_0 is the initial SOC, Q_N is the normal capacity of the battery, and η is the charging and discharging efficiency of the battery.

The system state-space equations are discretized into

$$\begin{cases} U_e(k) = e^{-\tau/\tau_e}U_e(k-1) + R_e\left(1-e^{-\tau/\tau_e}\right)I(k-1), \\ U_d(k) = e^{-\tau/\tau_d}U_d(k-1) + R_d\left(1-e^{-\tau/\tau_d}\right)I(k-1), \\ \mathrm{SOC}(k) = \mathrm{SOC}(k-1) - \dfrac{\eta\tau}{Q_N}I(k-1). \end{cases} \tag{15}$$

where τ, τ_e and τ_d are the sampling periods satisfying

$$\begin{cases} \tau_e = R_e \cdot C_e, \\ \tau_d = R_d \cdot C_d. \end{cases} \tag{16}$$

Hence, the established discretized state-space equation of the battery system is as follows:

$$\begin{bmatrix} \mathrm{SOC}(k) \\ U_e(k) \\ U_d(k) \end{bmatrix} = \begin{bmatrix} 1 & 0 & 0 \\ 0 & e^{-\tau/\tau_e} & 0 \\ 0 & 0 & e^{-\tau/\tau_d} \end{bmatrix} \begin{bmatrix} \mathrm{SOC}(k-1) \\ U_e(k-1) \\ U_d(k-1) \end{bmatrix} + \begin{bmatrix} \dfrac{\eta\tau}{Q_N} \\ R_e\left(1-e^{-\tau/\tau_e}\right) \\ R_d\left(1-e^{-\tau/\tau_d}\right) \end{bmatrix} I(k-1) + w(k-1), \tag{17}$$

where $w(\mathrm{k}-1)$ is the model observation noise. The discretized state output voltage of the model is

$$U(k) = U_{\mathrm{OCV}}(k) + U_O(k) + U_e(k) + U_D(k) + v(k-1), \tag{18}$$

where $v(k-1)$ is the observation noise of terminal voltage.

3.2. SOC Estimation Based on AUKF. The key to the UKF is the unscented transform operation to transform the mean and covariance of the nonlinear system, avoiding linearization operations and retaining the high-order terms of the system. The UKF also improves the transmission accuracy of the system Gaussian density. Further, the AUKF iteratively corrects the system noise covariance and the observed noise covariance using maximum likelihood estimation and expectation maximization, resulting in better adaptability and better estimation results [30].

For a nonlinear discrete-time system, the state equation and the measurement equation are as follows:

$$\begin{cases} x_k = f\left(x_{k-1}, u_{k-1}\right) + w_{k-1}, \\ y_k = h\left(x_k, u_k\right) + v_k, \end{cases} \tag{19}$$

where x_k is the system state vector, y_k is the measurement vector, u_k is the known input vector, w_k is the process Gaussian noise, v_k is the measurement noise Gaussian, and $f(x_k, u_k)$ is a nonlinear measurement function. The AUKF for the battery SOC estimation is illustrated as follows:

Step 1: Initialization and state extension

$$\begin{cases} \hat{x}_0 = E[x_0], \\ P_0 = E\left[(x_0 - \hat{x}_0)(x_0 - \hat{x}_0)^T\right], \\ \hat{X}_0 = E[X_0] = E[\hat{x}_0, 0, 0], \\ P_{X,0} = E\left[\left(X_0 - \hat{X}_0\right)\left(X_0 - \hat{X}_0\right)^T\right], \end{cases} \tag{20}$$

where $\hat{X}_0$ and $P_{X,0}$ are the initial state estimate and error covariance matrix. The state vector X_k is defined as

$$X_k = \left[\ \mathrm{SOC}(k)\ \ U_e(k)\ \ U_d(k)\ \right]^T. \tag{21}$$

with the state variables SOC(k), U_e(k) and U_d(k).

Step 2: 2L + 1 sampling (Sigma) points establishment

$$\begin{cases} X_{0,k-1} = X_{k-1}, & i = 0, \\ X_{i,k-1} = X_{k-1} + \sqrt{(L+\lambda)P_{X,k-1}}, & i = 1 \sim L, \\ X_{i,k-1} = X_{k-1} + \sqrt{(L+\lambda)P_{X,k-1}}, & i = L+1 \sim 2L. \end{cases} \tag{22}$$

Step 3: The weight calculation

The calculation of the mean weight and covariance weight can be presented as

$$\begin{cases} W_0^{(m)} = \dfrac{\lambda}{n+\lambda}, \\ W_0^{(c)} = \dfrac{\lambda}{n+\lambda} + \left(1 - \alpha^2 + \beta\right), \\ W_i^{(m)} = W_i^{(c)} = \dfrac{\lambda}{2(n+\lambda)}, \quad i = 1, 2, \ldots 2L, \end{cases} \tag{23}$$

where $\lambda = \alpha^2 (n + \varsigma) - n$ is a scale parameter to eliminate the total prediction error, α determines the distribution of sigma points around $\widehat{X}$ and is usually a small positive value ranging from 1 to e^{-4}, ς takes values of 0 to 3-n generally, β is used to integrate the X prior estimation and generally selected to be 2, and $W_i^{(m)}$ and $W_i^{(c)}$ are weighting factors to calculate the mean and covariance of the i-th sigma point, respectively.

Step 4: State estimation time updating

$$\begin{cases} \widehat{X}_{i,k} = f\left(X_{i|k-1}, u_{k-1}\right), \quad i = 0, 1, \ldots 2L, \\ X_{k|k-1} = \sum_{i=0}^{2L} W_i^{(m)} \widehat{X}_{i,k-1}. \end{cases} \tag{24}$$

Step 5: Covariance matrix time updating

$$P_{X,k|k-1} = \sum_{i=0}^{2L} W_i^{(c)} \left(\widehat{X}_{i,k} - X_{k|k-1}\right)\left(\widehat{X}_{i,k} - X_{k|k-1}\right)^T + Q_{k-1}. \tag{25}$$

where Q_k is the covariance of the process Gaussian noise w_k. R_k is the covariance of measurement noise Gaussian v_k, without relationship between them.

Step 6: New sigma points attainment at time $k|k$-1

$$\begin{cases} X_{0,k|k-1} = X_{k|k-1}, \quad i = 0, \\ X_{i,k|k-1} = X_{k|k-1} + \sqrt{(L+\lambda) P_{X,k|k-1}}, \quad i = 1 \sim L, \\ X_{i,k|k-1} = X_{k|k-1} + \sqrt{(L+\lambda) P_{X,k|k-1}}, \quad i = L+1 \sim 2L. \end{cases} \tag{26}$$

Step 7: Measurement estimation

$$\begin{cases} \widehat{y}_{i,k|k-1} = h\left(X_{i,k|k-1}, u_k\right), \\ y_{k|k-1} = \sum_{i=0}^{2L} W_i^{(m)} y_{i,k|k-1}. \end{cases} \tag{27}$$

Step 8: Kalman gain matrix

$$K = P_{xy} \cdot \leq P_{yy}^{-1}, \tag{28}$$

where

$$\begin{cases} P_{yy,k|k-1} = \sum_{i=0}^{2L} W_i^{(c)} \left(\widehat{y}_{i,k|k-1} - y_{k|k-1}\right)\left(\widehat{y}_{i,k|k-1} - y_{k|k-1}\right)^T + R_{k-1}, \\ P_{xy,k|k-1} = \sum_{i=0}^{2L} W_i^{(c)} \left(X_{i,k|k-1} - \widehat{X}_{k|k-1}\right)\left(\widehat{y}_{i,k|k-1} - y_{k|k-1}\right)^T. \end{cases} \tag{29}$$

Step 9: Residual calculating

$$\varepsilon_k = y_k - y_{k|k-1}. \tag{30}$$

Step 10: State estimation measurement updating

$$X_k = \widehat{X}_{k|k-1} + K\left(\varepsilon_k\right). \tag{31}$$

Step 11: Covariance matrix measurement updating

$$P_k = P_{k|k-1} - K \cdot P_{yy} \cdot K^T. \tag{32}$$

The above steps constitute the UKF. The AUKF contains an additional step to adjust the process noise covariance and measurement noise as follows.

Step 12: Adaptive adjustment of Q and R

The two noise covariance matrices are updated at each iteration using the following two equations in real time:

$$\begin{cases} Q_k = Q_{k|k-1} + K \cdot \varepsilon_{k-1} \cdot K^{-1} + P_k - \sum_{i=0}^{2L} W_i^{(c)} \left(\widehat{X}_{i,k} - X_{k|k-1}\right)\left(\widehat{X}_{i,k} - X_{k|k-1}\right)^T, \\ R_k = R_{k|k-1} + \varepsilon_{k-1} + \sum_{i=0}^{2L} W_i^{(c)} \left(X_{i,k|k-1} - \widehat{X}_{k|k-1}\right)\left(\widehat{y}_{i,k|k-1} - y_{k|k-1}\right)^T. \end{cases} \tag{33}$$

4. Equalization Control Algorithm

When discharged to a low SOC, the battery voltage decreases sharply [18, 31]. If the current is high, the battery may be damaged because of staying over-discharging for a long time. Likewise, when the battery is charged to a high SOC, its voltage increases significantly. When charged with a high current, the battery can be overcharged for a long time [32]. Besides, the polarization and ohmic effect are more significant if the battery ages severely, resulting in a more pronounced voltage drop at low SOC and voltage rise at high SOC [33–36]. Thus, adopting SOC as the single equalization criterion is not enough; this cannot prevent possible battery damage from overcharging and over-discharging [12, 37, 38].

Figure 7 is the SOC-OCV characteristic curve of the LIB. Assume that the interval [0.2, 0.8] denotes the SOC value between 0.2 and 0.8, which is considered as the plateau region. The intervals [0, 0.2] and [0.8, 1] are called non-platform interval where the SOC and OCV are approximately linear, and the terminal voltage can be measured online with a simple monitoring system. However, the OCV has little change in the plateau region. Thus, the terminal voltage and SOC are both chosen as the equalization parameters in this paper. The SOC-based equalization control algorithm is used when the SOC is in [0.2, 0.8], while the terminal-voltage-based equalization control algorithm is used when the SOC is below 0.2 or above 0.8. Unfortunately, there are various imbalance states; we cannot use the average SOC as an absolute benchmark for the SOC-based equalization algorithm. Figure 8 shows two battery packs in the imbalanced state. The average SOCs of both battery packs are between 0.2 and 0.8. However, in the battery pack shown in Figure 8(a), there is one cell with low SOC and others with high SOC that are at risk of overcharging. In the battery pack shown in Figure 8(b), there is one cell with high SOC and others with low SOC that needs to avoid over-discharging. Thus, this paper also proposes the SOC difference as another equalization parameter in the SOC-based equalization control algorithm. Similarly, the terminal-voltage-based equalization algorithm adopts the average and difference of terminal voltage between cells as equalization parameters. The specific implementation flow can be seen in Figure 9 where AFNN is an equalization control algorithm based on equalization parameters.

The equalization strategy is developed on the basis of the equalization circuit to optimize the performance of the equalization circuit, so that the overall equalization performance can be maximized [39]. However, controlling the magnitude of the equalization current is a very complex nonlinear control problem. Model neural networks (NNs) can achieve nonlinear mapping with arbitrary accuracy. However, the NN requires a large amount of data to train. In this paper, an adaptive fuzzy neural network is used to control the value of the equalization current in the equalization process.

The AFNN algorithm is combined with fuzzy logic control (FLC) and neural network to achieve high self-adaptability and good fault tolerance. The AFNN can adjust

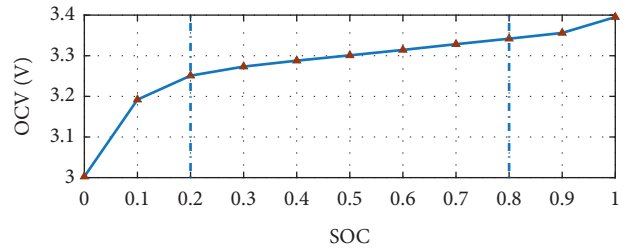

Figure 7: OCV versus SOC characteristic of the experimental LIB cell.

the membership function parameters as well as the weights between neurons [40]. In the paper, the AFNN is a first-order Takagi-Sugeno (T-S) fuzzy neural network based on the hybrid algorithm based on BP and least squares. It requires learning to determine five parameters including the antecedent and posterior parameters. The antecedent parameters of the network are obtained by BP algorithm, and the posterior parameters are identified by least squares, which greatly improves the learning efficiency. The AFNN is divided into five layers, including a fuzzy layer, a fuzzy rule intensity release layer, a rule strength normalization layer, a fuzzy rule output layer, and an output layer, as shown in Figure 10. The AFNN rules are obtained from the expert knowledge during equalization. The expert knowledge improves the reliability of the algorithm [41–43].

Layer 1. Fuzzy layer

There are two inputs to the fuzzy layer. For the SOC-based fuzzy neural network, the two inputs are $\triangle SOC$ and $\mathrm{SOC}_{\mathrm{avg}}$, which can be expressed as

$$\begin{cases} \Delta\mathrm{SOC} = \dfrac{\sum_{i=1}^{m}\mathrm{SOC}_i}{m} - \dfrac{\sum_{j=1}^{n}\mathrm{SOC}_j}{n}, \\ \mathrm{SOC}_{\mathrm{avg}} = \dfrac{\sum_{i=1}^{m}\mathrm{SOC}_i + \sum_{j=1}^{n}\mathrm{SOC}_j}{m+n}, \end{cases} \tag{34}$$

where SOC_i is the SOC of the i-th cell among the m cells on the left-hand side of the equalization unit, SOC_j is the SOC of the j-th cell among the n cells on the right-hand side of the equalization unit, ΔSOC denotes the difference between the average SOC of the cells on the left-hand side of the equalization unit and the average SOC of the cells on the right-hand sides of the equalization unit, and $\mathrm{SOC}_{\mathrm{avg}}$ denotes the average SOCs of all cells in the equalization unit.

For the terminal-voltage-based fuzzy neural network, the two inputs are the terminal-voltage difference ΔV and the terminal-voltage average V_{avg}, which can be presented as follows:

$$\begin{cases} \Delta V = \dfrac{\sum_{i=1}^{m}V_i}{m} - \dfrac{\sum_{j=1}^{n}V_{jj}}{n}, \\ V_{\mathrm{avg}} = \dfrac{\sum_{i=1}^{m}V_i + \sum_{j=1}^{n}V_j}{m+n}, \end{cases} \tag{35}$$

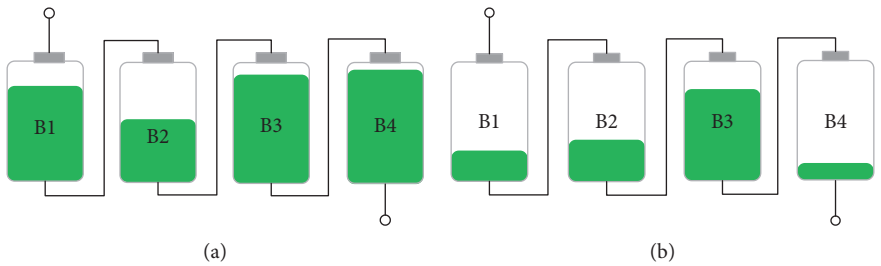

Figure 8: (a) Imbalanced SOC with one cell of low SOC and others of high SOC; (b) imbalanced SOC with one cell of high SOC and others of low SOC.

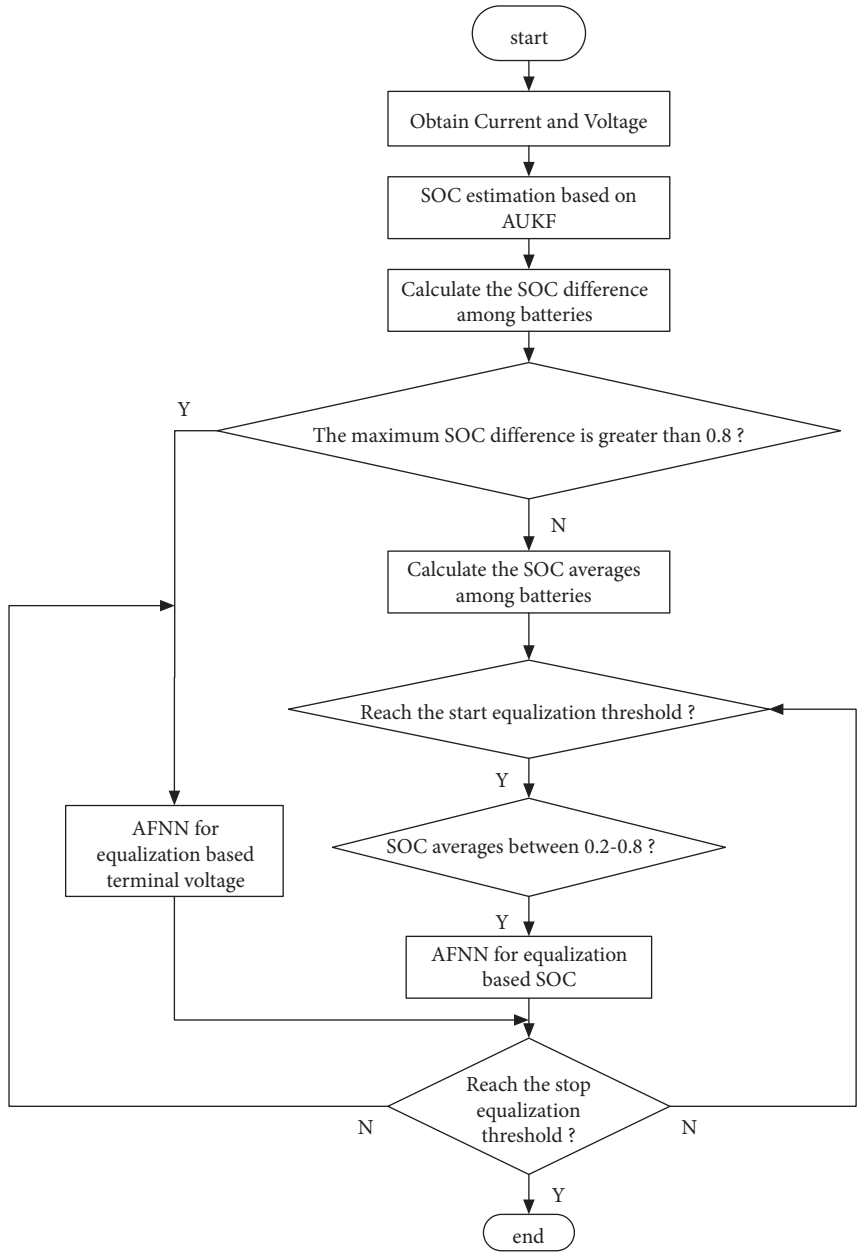

Figure 9: Flow chart of the equalization control strategy.

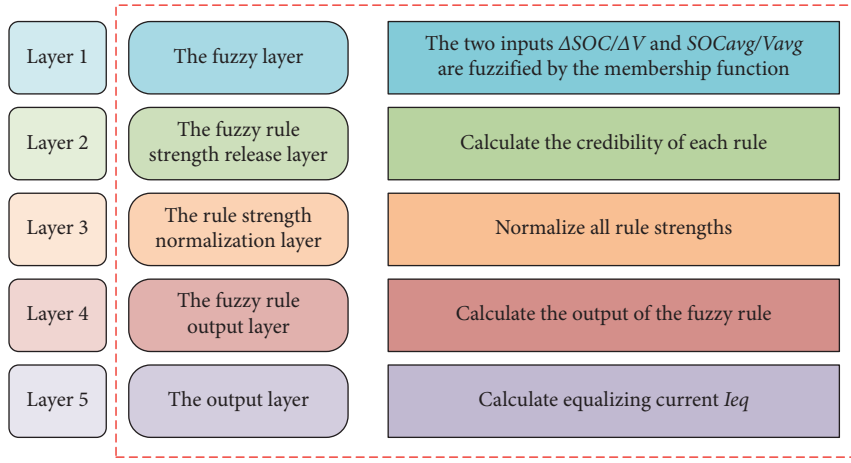

Figure 10: Structure of the adaptive fuzzy neural network.

where the ΔV represents the difference between the average terminal voltage of the cells on the left-hand side of the equalization unit and the average terminal voltage of the cells on the right-hand side of the equalization unit, and V_{avg} is the average terminal voltage of all cells in the equalization unit.

Furthermore, the equalization loss [44] of the battery is

$$E_L = \frac{\sum_{i=1}^{n} E_i^{\text{before}} - \sum_{i-1}^{n} E_i^{\text{after}}}{\sum_{i=1}^{n} E_i^{\text{before}} - \overline{E}^{\text{before}}} = \frac{\sum_{i=1}^{n} SOC_i^{\text{before}} - \sum_{i=1}^{n} SOC_i^{\text{after}}}{\sum_{i=1}^{n} SOC_i^{\text{before}} - \overline{SOC}^{\text{before}}}, \tag{36}$$

where E_L is the total energy consumption of the battery, E_i^{before} is the energy of the i-th battery cell before equalization, E_i^{after} denotes the energy of the i-th cell after equalization, and $\overline{E}$ is the average energy of all battery cells.

The number of fuzzy sets of the input parameters determines the number of membership functions in the first layer. The theoretical domain of ΔSOC is 0–0.6, SOC_{avg} is in 0–1, ΔV is in 0 to 1, and V_{avg} is in 2.6–4.2. In terms of the imbalanced state of the battery and characteristics, the theoretical domain of the inputs is divided into five fuzzy sets of very large (VL), large (L), medium (M), small (S), and very small (VS). A fuzzy rule base is developed through expert knowledge of the battery equalization control process and practical experience. Finally, the number of membership functions is obtained. The membership functions selected are all Gaussian functions, denoted as

$$\mu(x) = e^{-(x-a/b)^2}, \tag{37}$$

where a is the center of the membership function, b is the width of the membership function, and a and b, as antecedent parameters of the fuzzy neural network, are obtained via database training and learning.

The input parameters, $\Delta\text{SOC}/\Delta V$ and $\text{SOC}_{\text{avg}}/V_{\text{avg}}$, are defined as x_1 and x_2, respectively. The input and output of the first layer are

$$\begin{cases} O_i^1 = \mu_{A_i}(x_1), & i = 1, 2, \ldots 5, \\ O_j^1 = \mu_{B_j}(x_2), & j = 1, 2, \ldots 5, \end{cases} \tag{38}$$

where $\mu_{Ai}(x_1)$ is i-th membership function of input parameter x_1, and $\mu_{Bj}(x)$ is the j-th membership function of input parameter x_2.

Layer 2. Fuzzy rule intensity release layer

The output value can be calculated by

$$O_k^2 = \omega_k = \mu_{A_i}(x_1)\mu_{B_j}(x_2), \quad k = 1, 2, \ldots 25, \tag{39}$$

where ω_k represents the activation strength of one of the fuzzy rules.

Layer 3. Rule strength normalization layer

By calculating the weight of the activation strength for each fuzzy rule, the output of the layer is given by

$$O_k^3 = \overline{\omega_k} = \frac{\omega_k}{\sum_{k=1}^{25} \omega_k}. \tag{40}$$

Layer 4. Fuzzy rule output layer

The output of each fuzzy rule can be expressed as

$$\begin{aligned} O_k^4 &= \overline{\omega_k} f_k \\ &= \overline{\omega_k}(p_k x_1 + q_k x_2 + r_k), \end{aligned} \tag{41}$$

where p_k, q_k and r_k are used as the posterior parameters of the fuzzy neural network and are obtained by training.

Layer 5. Output layer

The layer is used to calculate the output equalization current value by

$$I_{eq} = O^5 = \sum_{k=1}^{25} \overline{\omega_k}. \quad (42)$$

5. Experimental Tests

Figure 11, a photograph of the experimental setup and associated instruments, is built as the core of experimental test, and the designing of software and hardware is given.

Subsection 5.1 is done in simulation with estimating the parameters in the second-order RC model and assessing the proposed AUKF in estimating the SOC, using the EKF and CKF as benchmarks. Meanwhile, Subsections 5.2 and 5.3 are based on the hardware experimental platform, including a DC supply power, a host computer, an active equalization controller, six serial connected batteries, an equalization circuit board, and an oscilloscope. For the active equalization controller, the MOSFET switch array is used to generate a pair of PWM signal for the MOSFETs to control the equalization circuit [45, 46]. The oscilloscope shows the control waveform of the inductors, which can be seen specifically in Figure 5 sawtooth wave, completing the equalization monitoring and characterizing the process of energy transfer. The sensors receive the voltage and current information of the batteries and send them to the host computer. The host computer uses these collected data for SOC estimation, monitoring cell voltage and string temperature, and protecting the whole equalization system [47].

5.1. SOC Accuracy Validation. We aim to estimate five parameters in the second-order RC model, i.e., *Re*, *Ce*, *Rd*, *Cd*, *R*0. They describe the dynamic behavior of the battery. First of all, we use a specific type of the LIB as the experimental object and analyze the Hybrid Pulse Power Characterization (HPPC) of the battery to obtain the pulse discharge current (as shown in Figure 12) and voltage data. The Parameter Estimation toolbox in MATLAB is then employed to estimate the five parameters. The estimation results conducted on a computer with Intel (R) Core (TM) i7-6700 CPU @ 3.40 GHz 3.41 GHz are shown in Figure 13. With these parameter estimates, a second-order RC equivalent model is built in MATLAB/Simscape.

We next compare the AUKF algorithm, the EKF, and the CKF in terms of their accuracy in estimating the SOC. The current values in Figure 12 are used as the inputs for the built equivalent circuit model. Figure 14(a) and Figure 14(b) present the error curves of the three methods. Table 1 summarizes the mean and standard variances of the errors generated by the three methods. We see that the estimation errors of both the EKF and CKF are larger than the estimation error of the AUKF. The AUKF converges faster, and the error tends to 8% in this condition. There is little doubt that the EKF is simple and suitable for nonlinear systems with a low degree; however, higher order terms of the EKF are ignored, and the filtering accuracy can be immensely reduced. The CKF has high filtering accuracy and

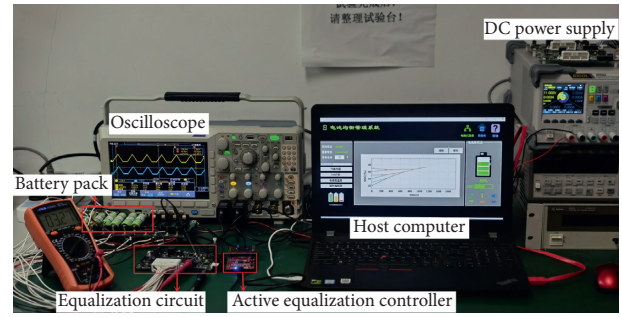

Figure 11: Photograph of the experimental setup and associated instruments.

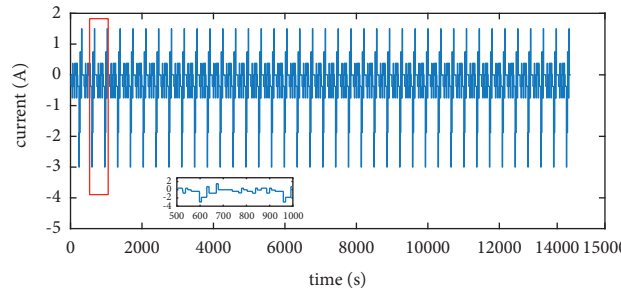

Figure 12: Dynamic stress test (DST) conditions.

good convergence, and yet some of the approximation errors are discarded when estimating the nonlinear system. When it comes down to it, however, the shortcomings of the CKF algorithm may make the filtering fail to meet the proposed consistency, and thus, the state truth cannot be estimated accurately. Sometimes there is also a problem of open-square failure, or even it is scattered when the degree of nonlinearity is high, or the initial error is large. With the advantages of UKF, no linearization error is introduced, and the accuracy can reach the second-order accuracy of Taylor series expansion without calculating Jacobi matrix. However, when the a priori noise statistical properties do not match the actual noise statistical properties, the state estimation performance of the UKF will be poor or even scattered. In the paper, the AUKF can adaptively adjust the process noise variance and measurement noise variance to reduce the model estimation error and suppress the filter divergence [48].

5.2. Performance Evaluation of the Proposed MLDIEC. To analyze the performance of the proposed MLDIEC, we compare it with three other battery equalization circuits: CIEC, PAEC, and DIEC. A comparison between these circuits is carried out in the standing, charging, and discharging states of the battery. The equalization efficiency is measured by two metrics: equalization time and energy loss. The initial values of SOC are listed in Table 2. The equalization loss of the battery pack is calculated by equation (38). It is significant to note that the energy losses during experiment will be smaller than that in the actual situation for several reasons. For example, line resistance is often

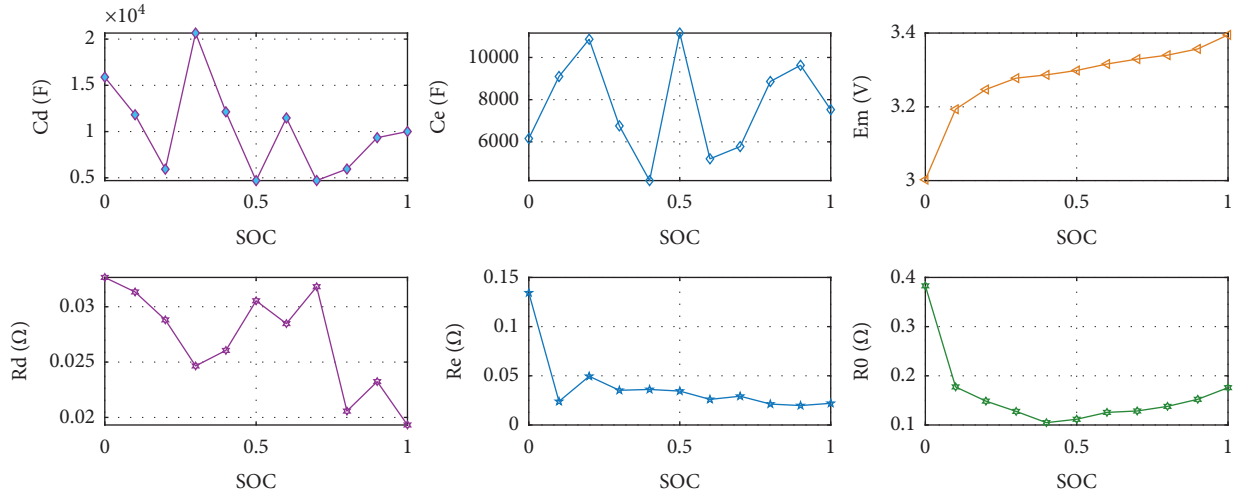

Figure 13: Model parameter estimation result.

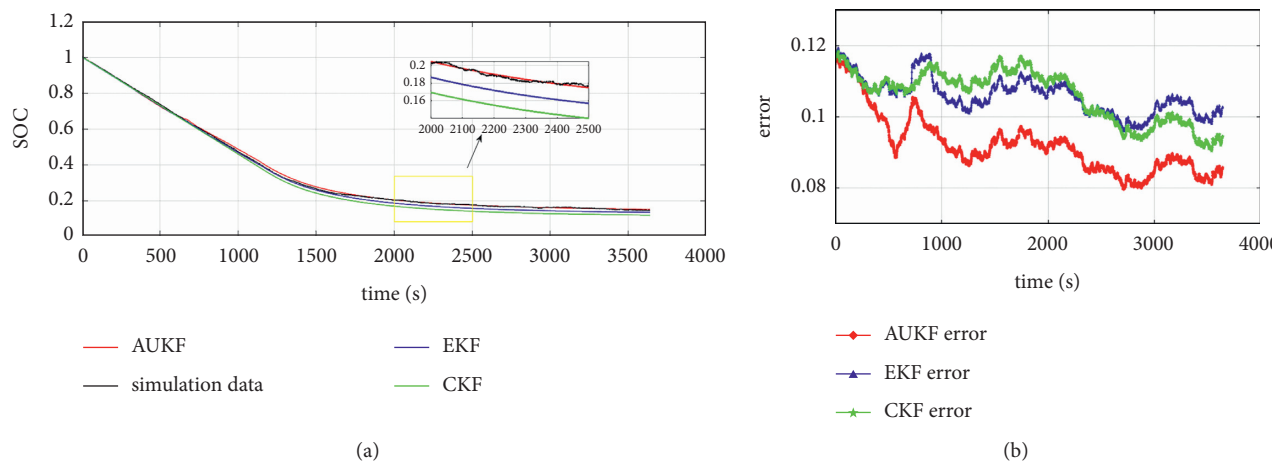

Figure 14: (a) SOC estimation results based on AUKF, EKF, and CKF; (b) errors of AUKF, EKF, and CKF in estimating SOC.

Table 1: Summary statistics of the SOC estimation result of the three Kalman filter methods.

SOC estimation method	EKF	CKF	AUKF
Mean error	0.01179	0.02378	−0.002665
Standard variance of the error	0.006076	0.01183	0.006611

Table 2: The initial SOCs of the six battery cells.

Battery cell	*B*1	*B*2	*B*3	*B*4	*B*5	*B*6
Initial SOC (%)	42	43	44	45	46	47

neglected. However, this will not affect the magnitude order of energy loss of the four equalization circuits, and thus, the comparisons are still meaningful.

Tables 3–5 present the equalization processes of the four equalization circuits in the three states, respectively. The horizontal coordinate is the equalization time, and the vertical one indicates the SOC. The CIEC has cumbersome energy transfer paths and unoptimized equalization units. Hence, its equalization time and energy losses are significantly higher than others. The DIEC adopts the dual parallel method that increases the equalization time by a factor of about one, while the energy can only be transferred between adjacent cells. The PAEC adds a high-level equalization unit to avoid the energy transfer disadvantage of the DIEC. As a result, the equalization time is shorter, and energy losses are lower. The proposed MLDIEC combines the advantages of the PAEC and DIEC. However, it should be noted that because the MLDIEC adopts the dual interleaved inductors that inevitably increase the energy loss from internal resistance of the battery, the energy loss of MLDIEC is slightly higher than that of PAEC. The equalization time and energy loss of the four equalization circuits under the same conditions are given in Figures 15 and 16, respectively. We see that the MLDIEC significantly reduces the energy loss and equalization time at the same time.

5.3. Performance Evaluation of the Proposed MLDIEC. The network model in this paper is constructed in the fuzzy toolbox in MATLAB, and the network design is

Table 3: Equalization results of the four equalizing circuits in the standing state.

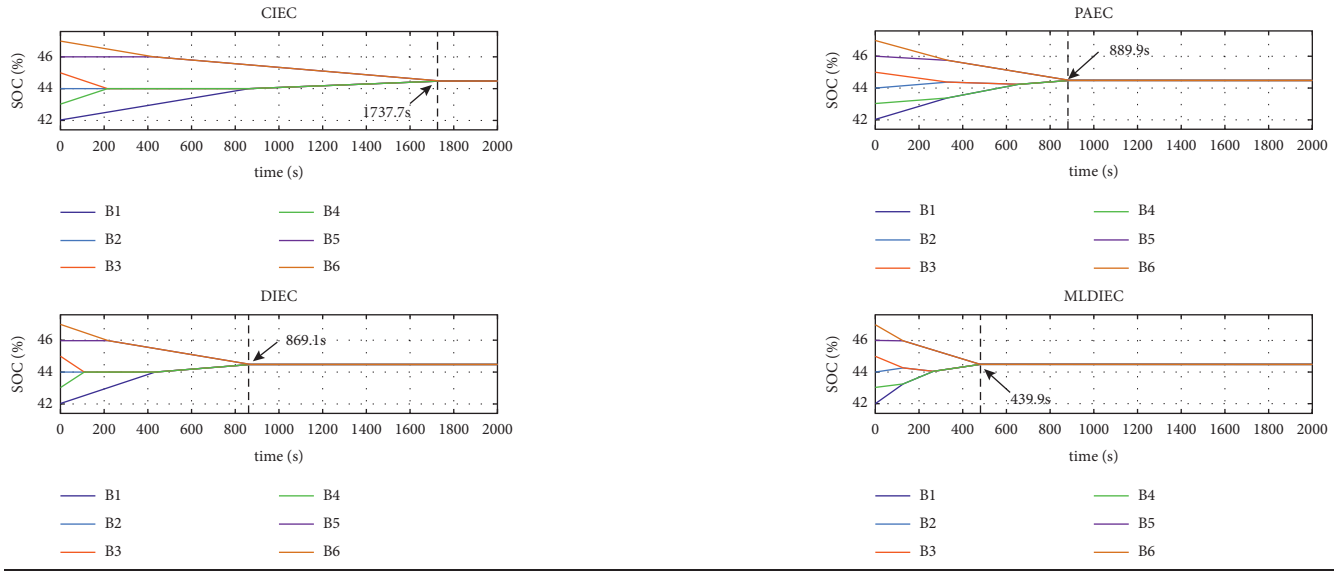

Table 4: Equalization results of the four equalizing circuits in the charging state.

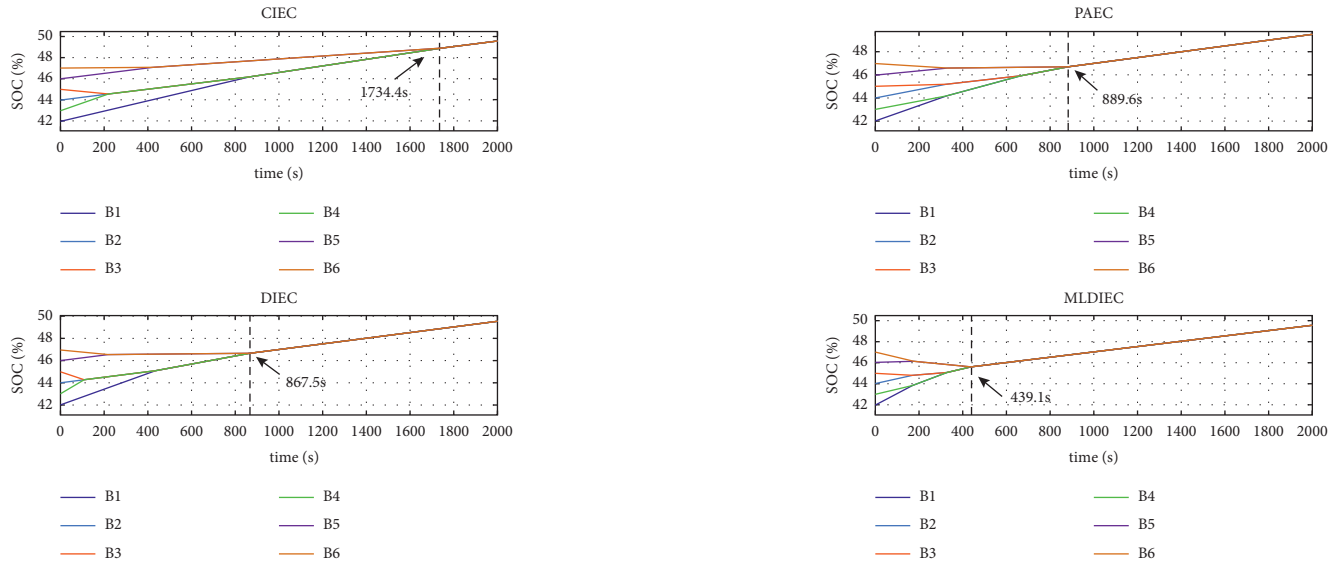

completed in three steps: training data import, generation of T-S fuzzy inference system, and learning algorithm selection and training. The generation of the T-S fuzzy inference system and the learning algorithm selection have been described in Section 4. The training data in the network are obtained from the battery characterization and the variation of the battery parameters in the experiment. The values of the antecedent parameters in the network are determined, and the membership functions of the 2 input quantities ($\triangle$SOC and SOC_{avg}) are clarified, as shown in Figure 17. Table 6 shows the 25 groups of 75 identification parameters. The switching surface of the AFNN output corresponding to the input is shown in Figure 18.

To test and verify the proposed equalization algorithm—the AFNN—for battery equalization, a comparison is made with the mean-difference algorithm in the standing, charging, and discharging state, as shown in Table 7. Note that, to emphasize the advantages of the AFNN for battery equalization, the differences of initial SOC between cells are set extremely large. We see that the AFNN improves the equalization times by 35.3%, 39.9%, and 37.1% compared with the mean-difference algorithm in the standing, charging, and discharging states, respectively. Meanwhile, the AFNN decreases the equalization energy losses by 4.9%, 4.4%, and 5.3% compared with the mean-difference algorithm in the standing, charging, and discharging states, respectively. The results of the two algorithms are summarized in Figure 19 to facilitate the comparison.

Table 5: Equalization results of the four equalizing circuits in the discharging state.

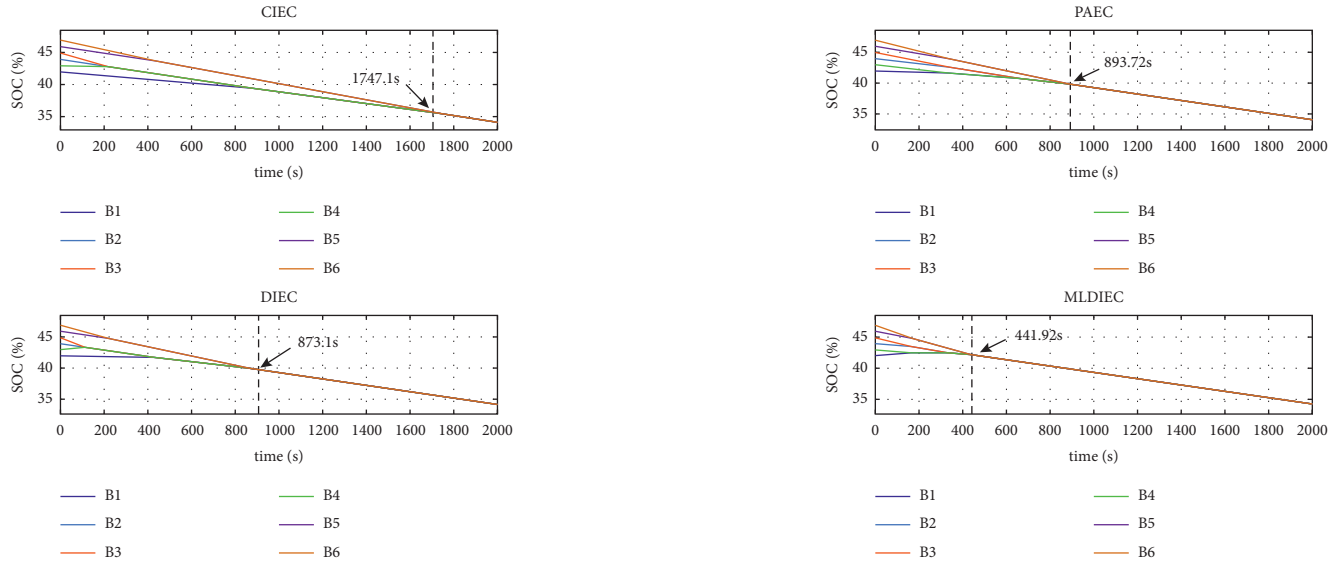

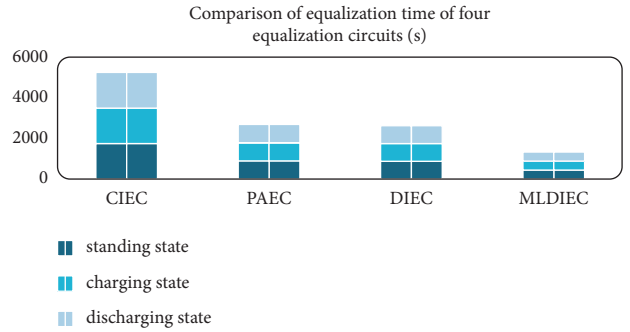

Figure 15: Comparisons of equalization time of the four equalization circuits.

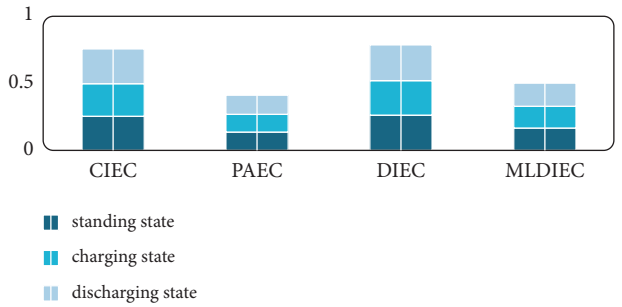

Figure 16: Comparisons of energy loss of the four equalization circuits.

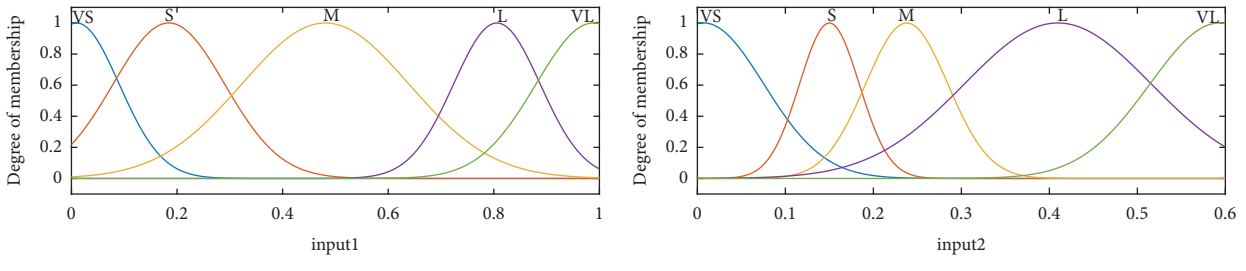

Figure 17: Membership function of the AFNN (a) SOC_{avg} (b) $\triangle SOC$.

Table 6: Output node.

Node	[P Q R]	Node	[P Q R]
O1	[−0.2043, 4.592, 0.687]	O14	[−0.9794, 0.1179, 2.26]
O2	[4.73, 4.666, 0.7763]	O15	[−0.9656, 0.4559, 2.005]
O3	[−8.91, −0.3964, 1.976]	O16	[−0.7007, −1.053, 1.295]
O4	[−0.6012, 3.246, 1.021]	O17	[5.141, 6.515, −4.145]
O5	[0.4065, 1.661, 1.983]	O18	[−5.866, −2.445, 6.494]
O6	[-0.1581, 4.431, 0.7461]	O19	[0.6098, 1.579, 0.2385]
O7	[−0.2639, 1.239, 1.222]	O20	[0.536, 2.706, −0.2429]
O8	[−1.508, 6.958, 0.245]	O21	[−0.5077, 3.491, 0.8377]
O9	[−5.737, 0.6068, 3.128]	O22	[0.06906, −0.3967, 0.7745]
O10	[−4.146, 0.1816, 2.808]	O23	[0.173, 6.92, −1.074]
O11	[0.02749, 4.017, 0.6894]	O24	[−1.84, 0.1639, 3.056]
O12	[−0.9279, 3.133, 1.288]	O25	[−0.06897, −0.4748, 1.599]
O13	[0.1818, 5.581, −0.2427]		

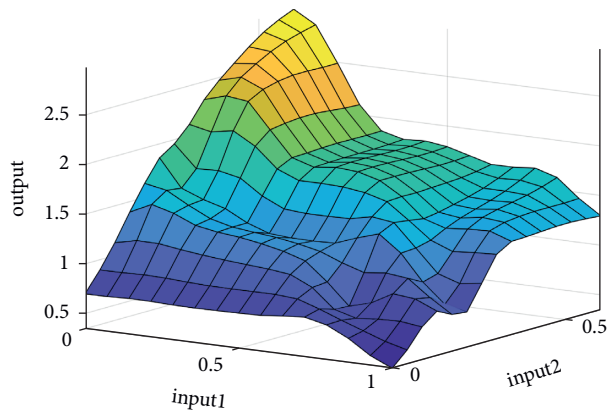

Figure 18: Switching surface of the AFNN output corresponding to the input.

Table 7: Equalization time comparison between mean-difference and AFNN algorithm in three states.

	Mean-difference algorithm	AFNN algorithm
Standing	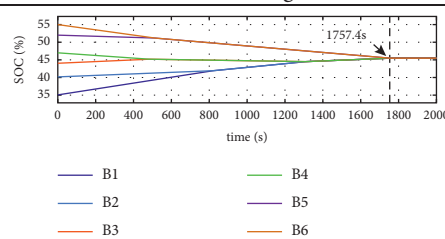	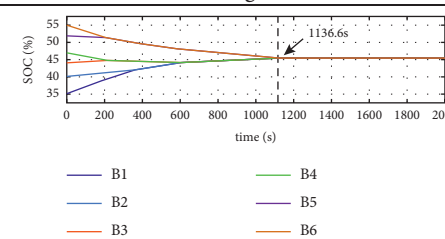
Charging	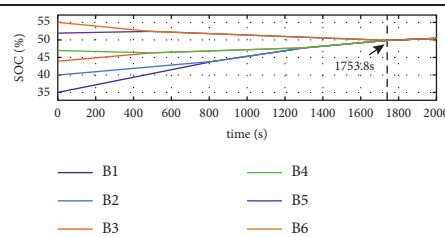	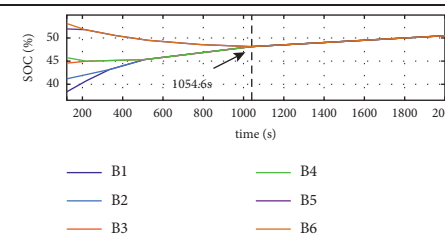
Discharging	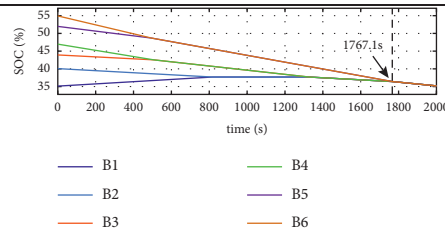	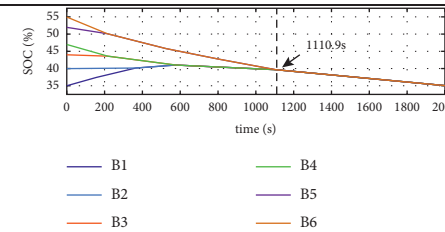

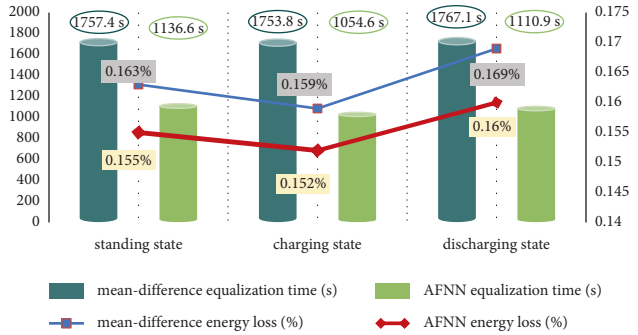

Figure 19: Equalization results based on mean-difference algorithm and AFNN algorithm in the three states.

6. Conclusion

This paper presents an AFNN-based multideck dual interleaved inductor active equalization circuit to reconcile the inconsistency of series-connected LIBs. The circuit provides an optimal path and energy transfer scheme between two nonadjacent cells by a high-level equalization unit. Dual inductors replace the single inductor in the equalization unit, allowing a cell to operate twice in one equalization cycle and avoiding the battery to be idle for a long time. Comparisons with other three equalization circuits show that the proposed equalization structure can greatly accelerate the equalization speed and reduce the equalization loss. The SOC and terminal voltage are chosen as the equalization criterion in different intervals of the SOC-OCV characteristic curve of LIBs, and the AUKF is used for SOC estimation. The AFNN algorithm is employed for effective equalization. Experimental results show that the AFNN algorithm increases the equalization efficiency by about 4.89% and saves the equalization time by about 37.4% compared with the mean-difference algorithm under the same operating conditions. In the future, the battery pack model will be further developed and widely used with more accurate SOC estimation values and less computational burden.

Abbreviations

AFNN: Adaptive fuzzy neural network
AUKF: Adaptive unscented Kalman filter
BP: Back propagation
CIEC: Classical inductor equalization circuit
CKF: Cubature Kalman filter
DCM: Discontinuous conduction mode
DIEC: Dual interleaved equalization circuit
DST: Dynamic stress test
EKF: Extended Kalman filter
EV: Electric vehicle
FLC: Fuzzy logic controller
HPPC: Hybrid pulse power characterization
KCL: Kirchhoff law
KVL: Kirchhoff's voltage law
LIB: Lithium-ion battery
MCU: Microcontroller unit
MLDIEC: Inductor-based multi-layer dual interleaved equalization circuit
MLIEC: Multi-layer inductor equalization circuit
NN: Neural network
OCV: Open-circuit voltage
PAEC: Parallel architecture equalization circuit
PWM: Pulse width modulation
T-S: Takagi-Sugeno
UKF: Unscented Kalman filter.

Data Availability

We have presented the data in the form of tables in the paper.

Conflicts of Interest

The authors declare that there are no conflicts of interest regarding the publication of this paper.

Acknowledgments

This research was supported by the Key Research and Development Program of Shaanxi Province (grant numbers 2019ZDLGY15-04-02, 2018ZDCXL-GY-05-07-02, 2019GY-083, and 2019GY-059).

References

[1] K.-M. Lee, S.-W. Lee, Y.-G. Choi, and B. Kang, "Active balancing of Li-ion battery cells using transformer as energy carrier," *IEEE Transactions on Industrial Electronics*, vol. 64, no. 2, pp. 1251–1257, 2017.

[2] X. Chen, W. Shen, Z. Cao, and A. Kapoor, "A novel approach for state of charge estimation based on adaptive switching gain sliding mode observer in electric vehicles," *Journal of Power Sources*, vol. 246, no. 3, pp. 667–678, 2014.

[3] W. P. Diao, M. Pecht, and T. Liu, "Management of imbalances in parallel-connected lithium-ion battery packs," *Journal of Energy Storage*, vol. 24, Article ID 100781, 2019.

[4] B. Dong, Y. Li, and Y. Han, "Parallel architecture for battery charge equalization," *IEEE Transactions on Power Electronics*, vol. 30, no. 9, pp. 4906–4913, 2015.

[5] T. H. Phung, A. Collet, and J.-C. Crebier, "An optimized topology for next-to-next balancing of series-connected lithium-ion cells," *IEEE Transactions on Power Electronics*, vol. 29, no. 9, pp. 4603–4613, 2014.

[6] Z. Wu, R. Ling, and R. Tang, "Dynamic battery equalization with energy and time efficiency for electric vehicles," *Energy*, vol. 141, pp. 937–948, 2017.

[7] Y. J. Wang, R. L. Xu, C. J. Zhou, X. Kang, and Z. H. Chen, "Digital twin and cloud-side-end collaboration for intelligent battery management system," *Journal of Manufacturing Systems*, vol. 62, pp. 124–134, 2020.

[8] K. I. Hwu and H. P. Liu, "Series-type charger with output voltage automatically regulated and hot swap," *International Journal of Circuit Theory and Applications*, vol. 47, no. 4, pp. 633–639, 2018.

[9] M. A. Hannan, M. M. Hoque, P. J. Ker, R. A. Begum, and A. Mohamed, "Charge equalization controller algorithm for series-connected lithium-ion battery storage systems: modelling and applications," *Energies*, vol. 10, no. 9, p. 1390, 2017.

[10] Y. Huang, B. T. Tran, S. Asghari et al., "Experimental and optimization of material synthesis process parameters for improving capacity of lithium-ion battery," *International Journal of Energy Research*, vol. 42, no. 10, pp. 3400–3409, 2018.

[11] S. Shili, A. Hijazi, A. Sari, X. Lin-Shi, and P. Venet, "Balancing circuit new control for supercapacitor storage system lifetime maximization," *IEEE Transactions on Power Electronics*, vol. 32, no. 6, pp. 4939–4948, 2017.

[12] W. Diao, N. Xue, V. Bhattacharjee, J. Jiang, O. Karabasoglu, and M. Pecht, "Active battery cell equalization based on residual available energy maximization," *Applied Energy*, vol. 210, pp. 690–698, 2018.

[13] Y. L. Shang, Q. Zhang, N. X Cui, and C. H. Zhang, "A cell-to-cell equalizer based on three-resonant-state switched-capacitor converters for series-connected battery strings," *Energies*, vol. 10, no. 2, p. 206, 2017.

[14] J. Qi and D. D.-C. Lu, "A preventive approach for solving battery imbalance issue by using a bidirectional multiple-input c converter working in DCVM," *IEEE Transactions on Industrial Electronics*, vol. 64, no. 10, pp. 7780–7789, 2017.

[15] N. Swaminathan, S. Steinhorst, M. Lukasiewycz, M. Kauer, and S. Chakraborty, "Optimal dimensioning and control of active cell balancing architectures," *IEEE Transactions on Vehicular Technology*, vol. 68, no. 10, pp. 9632–9646, 2019.

[16] Q. Ouyang, J. Chen, J. Zheng, and Y. Hong, "SOC estimation-based quasi-sliding mode control for cell balancing in lithium-ion battery packs," *IEEE Transactions on Industrial Electronics*, vol. 65, no. 4, pp. 3427–3436, 2017.

[17] R. Velho, M. Beirao, M. D. Calado, J. Pombo, J. Fermeiro, and S. Mariano, "Management system for large li-ion battery packs with a new adaptive multistage charging method," *Energies*, vol. 10, no. 5, p. 605, 2017.

[18] J. C Lv, B. C. Jiang, X. L. Wang, Y. Liu, and Y. Fu, "Estimation of the state of charge of lithium batteries based on adaptive unscented kalman filter algorithm," *Electronics*, vol. 9, no. 9, p. 1425, 2020.

[19] X. L. Wang, K. W. E. Cheng, and Y. C. Fong, "Non-equal voltage cell balancing for battery and super-capacitor source package management system using tapped inductor techniques," *Energies*, vol. 11, no. 5, p. 1037, 2018.

[20] A. F. Moghaddam and A. Van den Bossche, "Alex, "An efficient equalizing method for lithium-ion batteries based on coupled inductor balancing," *Electronics*, vol. 8, no. 2, p. 136, 2019.

[21] M. Fu, C. Zhao, J. Song, and C. Ma, "A low-cost voltage equalizer based on wireless power transfer and a voltage multiplier," *IEEE Transactions on Industrial Electronics*, vol. 65, no. 7, pp. 5487–5496, 2018.

[22] D. Balthazar, C. Remy, D. Benjamin, A. Marot, I. Guyon, and M. Schoenauer, "Neural networks for power flow: graph neural solver," *Electric Power Systems Research*, vol. 189, Article ID 106547, 2020.

[23] N. Bouchhima, M. Schnierle, S. Schulte, and K. P. Birke, "Optimal energy management strategy for self reconfigurable batteries," *Energy*, vol. 122, pp. 560–569, 2017.

[24] Y. L. Shang, B. Xia, J. F. Yang, and C. Zhang, "A delta-structured Switched-Capacitor Equalizer for Series-Connected Battery Strings," in *Proceedings of the 2017 IEEE Energy Conversion Congress and Exposition (ECCE)*, pp. 4493–4496, Cincinnati, OH USA, October 2017.

[25] Z. B. Omariba, L. J. Zhang, and D. B. Sun, "Review of Battery Cell Balancing Methodologies for Optimizing Battery Pack Performance in Electric Vehicles," *IEEE Access*, vol. 7, pp. 129335–129352, 2019.

[26] Y. Ye and K. W. E. Cheng, "Analysis and design of zero-current switching switched-capacitor cell balancing circuit for series-connected battery/supercapacitor," *IEEE Transactions on Vehicular Technology*, vol. 67, no. 2, pp. 948–955, 2018.

[27] X. Tang, C. Zou, T. Wik et al., "Run-to-run control for active balancing of lithium iron phosphate battery packs," *IEEE Transactions on Power Electronics*, vol. 35, no. 2, pp. 1499–1512, 2020.

[28] K. Shimul, "Dam, vinod john, "low-frequency selection switch based cell-to-cell battery voltage equalizer with reduced switch count"," *IEEE Transactions on Industry Applications*, vol. 57, no. 4, pp. 3842–3851, 2021.

[29] Z. Shuzhi, G. Xu, and Z. Xiongwen, "An improved adaptive unscented kalman filtering for state of charge online estimation of lithium-ion battery," *Journal of Energy Storage*, vol. 32, Article ID 101980, 2020.

[30] W. Han, C. Zou, C. Zhou, and L. Zhang, "Estimation of cell SOC evolution and system performance in module-based battery charge equalization systems," *IEEE Transactions on Smart Grid*, vol. 10, no. 5, pp. 4717–4728, 2019.

[31] M. T. Huang, C. Wang, and J. M. Zhao, "State of charge estimation of lithium-ion battery based on second-order extended Kalman filter," in *Proceedings of the 2019 IEEE 4th Advanced Information Technology, Electronic and Automation Control Conference (IAEAC)*, pp. 335–338, Chengdu, China, December 2019.

[32] B. Li and S. Bei, "Estimation algorithm research for lithium battery SOC in electric vehicles based on adaptive unscented Kalman filter," *Neural Computing & Applications*, vol. 31, no. 12, pp. 8171–8183, 2019.

[33] X. G. Wu, Z. H. Cui, X. F. Li, J. Y. Du, and Y. Liu, "Control strategy for active hierarchical equalization circuits of series battery packs," *Energies*, vol. 12, no. 11, p. 2071, 2019.

[34] X. Tian, R. He, X. Sun, Y. Cai, and Y. Xu, "An ANFIS-based ECMS for energy optimization of parallel hybrid electric bus," *IEEE Transactions on Vehicular Technology*, vol. 69, no. 2, pp. 1473–1483, 2020.

[35] G. J. Meyer, T. Lorz, R. Wehner, J. Jaeger, M. Dauer, and R. Maximilian, "Hybrid fuzzy evaluation algorithm for power system protection security assessment," *Electric Power Systems Research*, vol. 189, Article ID 106555, 2020.

[36] Y. Wang, C. Zhang, Z. Chen, J. Xie, and X. Zhang, "A novel active equalization method for lithium-ion batteries in electric vehicles," *Applied energy*, vol. 145, pp. 36–42, 2015.

[37] A. Tavakoli, S. A. Khajehoddin, and J. Salmon, "Control and analysis of a modular bridge for battery cell voltage balancing," *IEEE Transactions on Power Electronics*, vol. 33, no. 11, pp. 9722–9733, 2018.

[38] X. D. Cui, W. X. Shen, Y. L. Zhang, and C. G. Hu, "A novel active online state of charge based balancing approach for lithium-ion battery packs during fast charging process in electric vehicles," *Energies*, vol. 10, no. 11, p. 1766, 2017.

[39] Y. Chen, X. Liu, H. K. Fathy, J. Zou, and S. Yang, "A graph-theoretic framework for analyzing the speeds and efficiencies of battery pack equalization circuits," *International Journal of Electrical Power & Energy Systems*, vol. 98, pp. 85–99, 2018.

[40] B. Wang, F. Qin, X. Zhao, X. Ni, and D. Xuan, *International Journal of Energy Research*, vol. 44, no. 6, pp. 4812–4826, 2020.

[41] D. J. Docimo and H. K. Fathy, "Multivariable state feedback control as a foundation for lithium-ion battery pack charge and capacity balancing," *Journal of the Electrochemical Society*, vol. 164, no. 2, pp. A61–A70, 2017.

[42] Y. Ma, P. Duan, Y. Sun, and H. Chen, "Equalization of lithium-ion battery pack based on fuzzy logic control in electric vehicle," *IEEE Transactions on Industrial Electronics*, vol. 65, no. 8, pp. 6762–6771, 2018.

[43] X. Lei, X. Zhao, G. P. Wang, and W. Y. Liu, "A novel temperature–hysteresis model for power battery of electric vehicles with an adaptive joint estimator on state of charge and power," *Energies*, vol. 12, no. 19, p. 3621, 2019.

[44] S.-J. Lee, M. Kim, Ju-W. Baek, D.-W. Kang, and J.-H. Jung, "Enhanced switching pattern to improve cell balancing performance in active cell balancing circuit using multi-winding transformer," *IEEE Access*, vol. 8, pp. 149544–149554, 2020.

[45] X. Qi, Yi Wang, Y. Wang, and Z. Chen, "Optimization of centralized equalization systems based on an integrated cascade bidirectional DC-DC converter," *IEEE Transactions on Industrial Electronics*, vol. 69, no. 1, pp. 249–259, 2021.

[46] Li Yu and J. Xu, "Xuesong mei, and junping wang "A unitized multiwinding transformer based equalization method for series-connected battery string"," *IEEE Transactions on Power Electronics*, vol. 34, no. 12, pp. 11981–11989, 2019.

[47] N. Ghaeminezhad, Q. Ouyang, X. Hu, and G. Xu, "Zhisheng wang "active cell equalization topologies analysis for battery packs: a systematic review"," *IEEE Transactions on Power Electronics*, vol. 36, no. 8, pp. 9119–9135, 2021.

[48] M. Preindl, "A battery balancing auxiliary power module with predictive control for electrified transportation," *IEEE Transactions on Industrial Electronics*, vol. 65, no. 8, pp. 6552–6559, 2018.